Enhanced photoelectrocatalytic hydrogen evolution using off-stoichiometry La 0.43 FeO y films

Vincent Guigoz, Stéphanie Bruyère, Sylvie Migot, Raphaël Schneider, Thomas Gries

Enhanced photoelectrocatalytic hydrogen evolution using off-stoichiometry $La_{0.43}FeO_y$ films

Vincent Guigoz [a,b], Stéphanie Bruyère[b], Sylvie Migot[b], Raphaël Schneider [a,*], Thomas Gries [b,*]

[a] *Université de Lorraine, CNRS, LRGP, F-54000 Nancy, France*

[b] *Université de Lorraine, CNRS, IJL, F-54000 Nancy, France*

* Corresponding authors.

E-mail addresses: raphael.schneider@univ-lorraine.fr; thomas.gries@univ-lorraine.fr

Abstract

In this work, the influence of the stoichiometry of La_xFeO_y films on their activity for H_2 production by photoelectrochemical (PEC) water splitting was investigated. Thin La_xFeO_y films were deposited on electrodes by magnetron co-sputtering and their composition was controlled by adjusting the power applied on metallic iron and lanthanum targets. The highest photoactivity was observed for $La_{0.43}FeO_y$ films. The crystallization of these films and their photocatalytic activity were further improved by oxidation in an external furnace at 650°C for 2 h. Transmission electron microscopy (TEM) analyses confirm the formation of $LaFeO_3$ crystallites in the film and show a thin continuous polycrystalline Fe_2O_3 layer at the surface. The presence of Fe_2O_3 at the upper surface originates from an exsolution mechanism typically observed for non-stoichiometric perovskites. The improvement of the photocatalytic properties by adjusting the stoichiometry, the oxidation temperature and the film thickness was confirmed by H_2 production measurements performed by mass spectrometry. We observe a large increase in H_2 production rate (103%) by comparison with a

stoichiometric $LaFeO_3$ thin film. The improvement in catalytic performances for these non-stoichiometric films composed of earth abundant, low-cost and non-toxic elements, make them of high interest materials for photoelectrodes in PEC water splitting systems.

Keywords : La_xFeO_y; off-stoichiometry; photoelectrochemical H_2 production

1. Introduction

As a respond to the global energy demand, hydrogen (H_2) appears to be a promising energy carrier to replace fossil fuels, if produced renewably [1,2]. Photoelectrochemical (PEC) water splitting is one of the most promising process to generate H_2 but the PEC efficiency is limited by the semiconductor photocatalyst performances [3–7]. Recently, perovskite materials with the general formula ABO_3 (A and B being cations) have attracted great attention as photocatalysts [8–11]. Due to the abundance of its components, its low toxicity and its optical absorption in the visible light range, lanthanum ferrite perovskite ($LaFeO_3$) was demonstrated to be a high value candidate for H_2 photoproduction [10,12–15]. However, its performances are limited by a high charge recombination rate due to the modest electron transport [10,16–20]. In recent years, various methods have been developed to improve the light absorption and the charge transport in $LaFeO_3$ photocatalysts such as the creation of heterojunctions, nanostructuration or doping [5,12,21–25].

Another option is the development of non-stoichiometric materials responding to the general formula $La_{1-x}FeO_y$. Indeed, various studies have demonstrated the interest of modifying the stoichiometry (La/Fe ratio) of $LaFeO_3$ for the catalytic conversion of gases such as NO or CO and of hydrocarbons [26–28]. The catalytic performances for the oxidation of CO, propene and CH_4 increase using $La_{1-x}FeO_y$ having an over-stoichiometry in Fe [26,29]. This increase is linked to the smaller particle size and thus to the higher specific surface area, as particle growth is slowed down by the excess in Fe. X-ray photoelectron spectroscopy (XPS) measurements of $La_{1-x}FeO_y$ particles also revealed the formation of a Fe_2O_3 phase on the surface of the particles [30]. Fe_2O_3 was demonstrated to generate crystal defects that promote the adsorption of oxygen on the

surface. The highest catalytic activity was observed for $La_{0.9}FeO_y$ in the oxidation of CH_4 and for Cu-doped $La_{0.67}Fe_{0.83}Cu_{0.17}O_3$ in the oxidation of CO and propene. However, a significant excess in Fe can no longer be accommodated on the surface of $La_{1-x}FeO_y$ and can generate surface defective layers containing stacking faults or displacive Fe leading to a decrease of catalytic activity [28]. Therefore, a fine tuning of the non-stoichiometric composition is of high importance to control the catalytic properties.

Herein, thin $La_{1-x}FeO_y$ films were engineered to demonstrate the increase in photocatalytic activity compared to $LaFeO_3$. The non-stoichiometric films were produced via the magnetron co-sputtering process and the deviation from the ideal ABO_3 stoichiometry was finely tuned by adjusting the powers applied to the La and Fe targets. First, the influence of the composition on the photocatalytic properties is demonstrated. Next, the improvement of the photocatalytic properties by optimization of the oxidation treatment and of the layer thickness is discussed. Finally, H_2 photoproduction by PEC water splitting under simulated solar illumination is presented to further support the enhanced photocatalytic activity of these $La_{1-x}FeO_y$ non-stoichiometric layers.

2. Experimental Section

2.1. Elaboration of $La_{1-x}FeO_y$ thin films

$La_{1-x}Fe$ films were deposited on fluorine doped tin oxide coated glass (FTO, TEC 7 $\Omega.sq^{-1}$) and silicon substrates by direct current (DC) magnetron co-sputtering of two metal targets: Fe target (diameter: 50 mm, thickness: 0.25 mm, purity: 99.5%) and La target (diameter: 50 mm, thickness: 3 mm, purity: 99.9%). The targets were powered by two Advanced Energy MDX 500 DC generators. A base pressure of 5×10^{-4} Pa in the sputtering chamber was provided by a mechanical and a turbo-molecular pump. The experimental device was equipped with two independent magnetrons focused on the centre of the substrate-holder with an inclination of 30° with respect to the substrate normal, and the target to substrate distance was set equal to 10 cm. Thin films were synthesized at a working pressure of 0.58 Pa in a 10 vol.% H_2 – 90 vol.% Ar mixture. The substrate-holder rotated at 28 rpm to ensure film homogeneity. Thin films were

deposited without external heating and the self-established deposition temperature was below 50°C. At this temperature, films remained amorphous and a post-annealing in a tubular furnace at 500°C for 2 h in air was conducted to obtain the perovskite structure.

2.2. Characterization

The La/Fe atomic ratio was estimated by energy dispersive spectrometry (EDS) coupled to a scanning electron microscope (SEM) FEI Quanta 650 FEG. Due to the uncertainty on the oxygen chemical contents measured by EDS, the La and Fe atomic concentrations were determined on metallic films, i.e. before annealing post-treatment. Film thicknesses were measured by SEM cross-section observation. Transmission electron microscopy (TEM) investigations were performed using a cold FEG JEOL ARM200 microscope operating at 200 kV and equipped with spherical aberration (Cs) probe and image correctors (point resolution 0.12 nm in TEM mode). High-angle annular dark field image in scanning TEM (HAADF-STEM) and 2D elemental mapping using energy dispersive X-ray spectroscopy (EDX) are combined to obtain information about elemental distribution along film thickness. For these analyses, cross-section TEM samples of films deposited on silicon substrates were prepared using a focus ion beam (FIB) – SEM dual beam system FEI Helios NanoLab 600i. X-ray diffraction (XRD) was performed at room temperature using Bragg-Brentano θ/2θ measurements on a D8 Advance Bruker diffractometer (Cu K_α, λ = 1.54056 Å). The average crystallite size can be estimated from the full-width at half-maximum of diffraction peaks using the Scherrer's formula after correction from the experimental broadening (Eq. 1):

$$d_{hkl} = \frac{0.9\lambda}{\beta_{hkl} cos\theta} \quad (1)$$

where d_{hkl} is the average grain size along the *hkl* reticular distance, λ is the X-ray wavelength, θ is the diffraction angle and β_{hkl} is the full-width at half-maximum of the diffraction peak. UV-visible absorption spectra were recorded on Cary 7000 UMS Agilent UV-visible spectrophotometer. Photoelectrochemical measurements of as-prepared samples were performed by a SP 150 BioLogic potentiostat connected to a standard three electrode cell: Pt wire as the counter electrode, a saturated Ag/AgCl electrode as reference electrode and FTO glass coated with $La_{1-x}FeO_y$ (1 cm × 1 cm) as the working electrode. A 0.1 M Na_2SO_4 (pH = 7) aqueous solution was used as

electrolyte. All measurements were carried out under light illumination of 1 sun (100 $mW \cdot cm^{-2}$) provided from a Xenon lamp (Newport Xe 300 W ozone free) fitted with an air mass filter (AM 1.5G). Linear sweep voltammetry (LSV) measurements were obtained by scanning the potential from -0.8 V to 0.1 V vs Ag/AgCl at a scan rate of 5 $mV.s^{-1}$. The photocurrent density was evaluated from chronoamperometric measurements recorded at a constant potential of -0.30 V vs the reference electrode by cycling between dark and light illuminations of 30 s each for 10 min. Electrochemical impedance spectra (EIS) measurements were performed in the same workstation by applying a sinusoidal AC perturbation of 10 mV with a frequency range from 500 kHz to 0.01 Hz.

2.3. Hydrogen photoproduction

The photocatalytic hydrogen production experiments were performed in a sealed custom-made metallic PEC cell with an attached quartz viewport using the same experimental conditions as described for PEC measurements. The system was purged with Ar for 1 h before measurements. The amounts of produced H_2 and O_2 were determined during the water splitting reaction using an online quadrupole mass spectrometer (MS, Inficon Transpector MPS 100) operating with Ar as carrier gas. Measurements were conducted at an interval of 1 h and averaged over 2 min.

3. Results

3.1. $La_{1-x}FeO_y$ films synthesis and characterization

The La/Fe atomic ratio in the as-deposited films can be tuned by changing the discharge power applied to the Fe and La targets. The experimental parameters and the film compositions are summarized in Table 1. Seven samples with over-stoichiometry in Fe were synthesized by progressively decreasing the power applied to the La target, the power applied to Fe target being fixed at 80 W: $La_{0.11}FeO_y$, $La_{0.25}FeO_y$, $La_{0.33}FeO_y$, $La_{0.43}FeO_y$, $La_{0.54}FeO_y$, $La_{0.66}FeO_y$ and $La_{0.82}FeO_y$. Two samples were also elaborated with La over-stoichiometry: $La_{1.26}FeO_y$ and La_4FeO_y. These samples will be compared to Fe_2O_3 and $LaFeO_3$ films. The depositions durations

were adjusted according to the sputtering rate of each target to keep the thickness constant after annealing, at about 500 nm.

Table 1: Deposition conditions, thickness and composition of $La_{1-x}FeO_y$ thin films synthesized by magnetron co-sputtering of La and Fe targets and annealed at 500°C for 2 h in air.

Power Fe (W)	Power La (W)	Deposition time (min)	Sample composition
80	0	19.5	Fe_2O_3
80	15	18	$La_{0.11}FeO_y$
80	30	16	$La_{0.24}FeO_y$
80	40	15	$La_{0.33}FeO_y$
80	45	14	$La_{0.43}FeO_y$
80	50	13	$La_{0.54}FeO_y$
80	55	12	$La_{0.66}FeO_y$
80	60	11	$La_{0.82}FeO_y$
80	65	10	$LaFeO_3$
60	65	9	$La_{1.26}FeO_y$
20	65	5	La_4FeO_y

Fig. 1 shows the XRD patterns of the as-synthesized thin films with different compositions. The dotted peaks correspond to the FTO-coated glass substrate. Depending on the film stoichiometry, the XRD patterns exhibit different crystal phases. Samples can be divided into 4 groups.

- Group 1 corresponds to the films with a high Fe excess: Fe_2O_3 and $La_{0.11}FeO_y$. Only peaks corresponding to Fe_2O_3 (rhombohedral hematite R-3c, PDF file 00-033-0664) could be observed.
- Group 2 corresponds to the films with an intermediate stoichiometry: $La_{0.24}FeO_y$, $La_{0.33}FeO_y$, $La_{0.43}FeO_y$ and $La_{0.54}FeO_y$. Despite the oxidation treatment at 500°C for 2 h in air, the films were found to be amorphous as observed in the XRD patterns with a broad peak between 20 and 40°.
- Group 3 corresponds to films prepared with La/Fe atomic ratios close to 1: $La_{0.66}FeO_y$ and $La_{1.26}FeO_y$. The corresponding XRD patterns can be indexed to the orthorhombic $LaFeO_3$ perovskite phase (Pnma, PDF file 04-011-7994).

- Group 4 corresponds to the deposit with a significant La over-stoichiometry: La_4FeO_y. The XRD pattern can be assigned to the cubic structure of lanthanum oxide La_2O_3 (Ia-3, PDF file 03-065-3185).

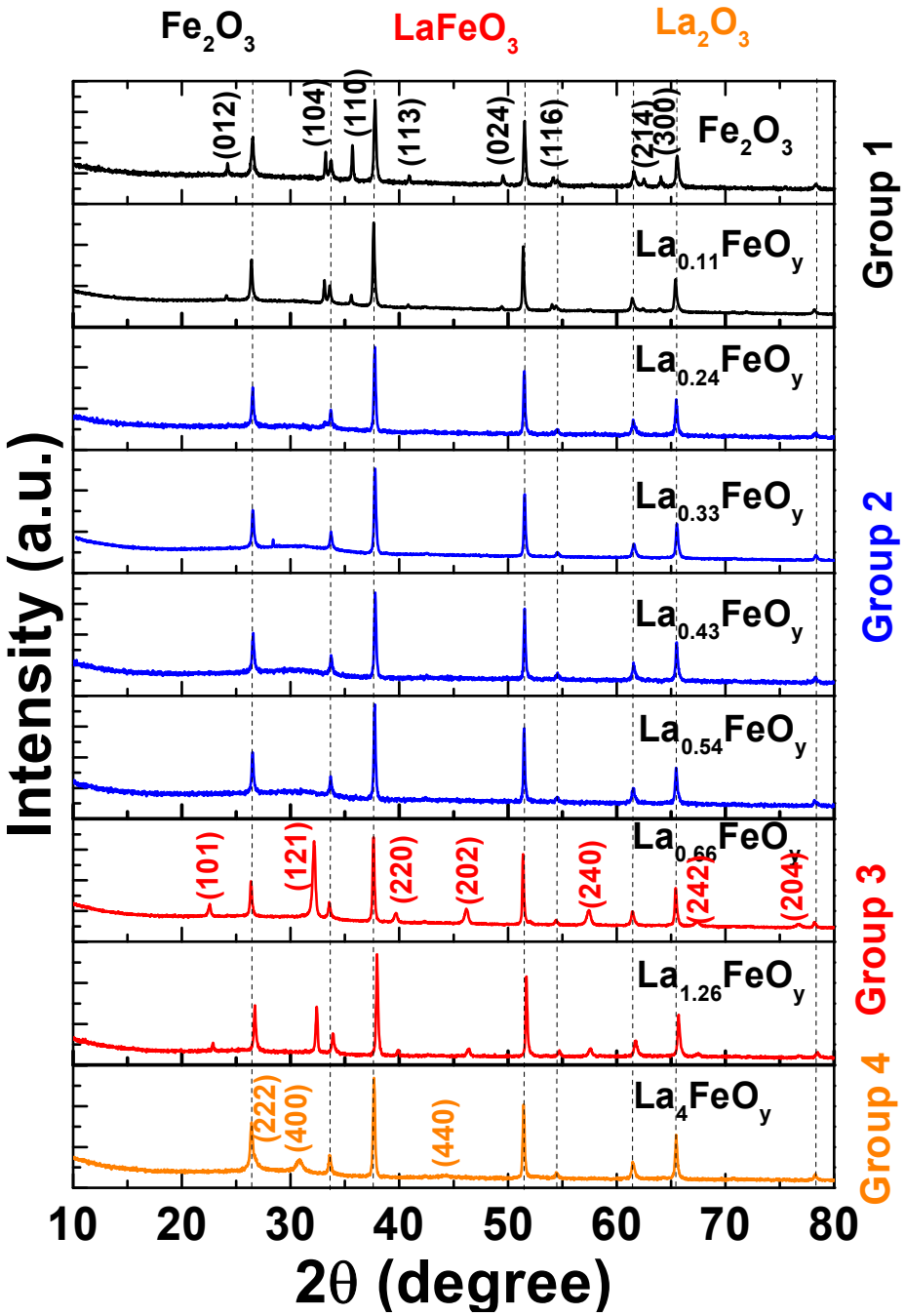

Fig. 1. Evolution of XRD patterns as a function of the sample composition after oxidation at 500°C for 2 h.

Fig. 2 shows the UV-visible absorption of the reference films ($LaFeO_3$ and Fe_2O_3), of the films with intermediate compositions ($La_{0.33}FeO_y$ and $La_{0.43}FeO_y$), of the film with near stoichiometric composition ($La_{0.82}FeO_y$) and of the film mainly composed of La_4FeO_y. The absorption of Fe_2O_3 shows a transition towards 550 nm. The optical bandgap energy was determined using Tauc plot and a value of 2.18 eV was obtained for an indirect allowed transition (Fig. S1b). A bandgap of ca. 2.28 eV was determined for $LaFeO_3$ thin films deposited in the same experimental conditions, from a direct forbidden transition [13]. These values are in good agreement with those reported in the literature [7,31]. The UV-visible absorption spectra of the three non-stoichiometric films (groups 2 and 3) have an intermediate behaviour relative to Fe_2O_3 and $LaFeO_3$ films. Furthermore, the nature of the transition does not seem to significantly influence the bandgap values of these intermediate non-stoichiometric films. For instance, for $La_{0.43}FeO_y$, an optical bandgap energy of 2.25 eV can be estimated from both indirect allowed and direct forbidden transitions (Fig. S1a and S1b). The absorption of the La_4FeO_y film markedly decreases at wavelengths above 350 nm, limiting its photocatalytic activity mostly to UV irradiation. This result can be correlated with the wide bandgap energy of La_2O_3 estimated to be 5.2 eV [32–36].

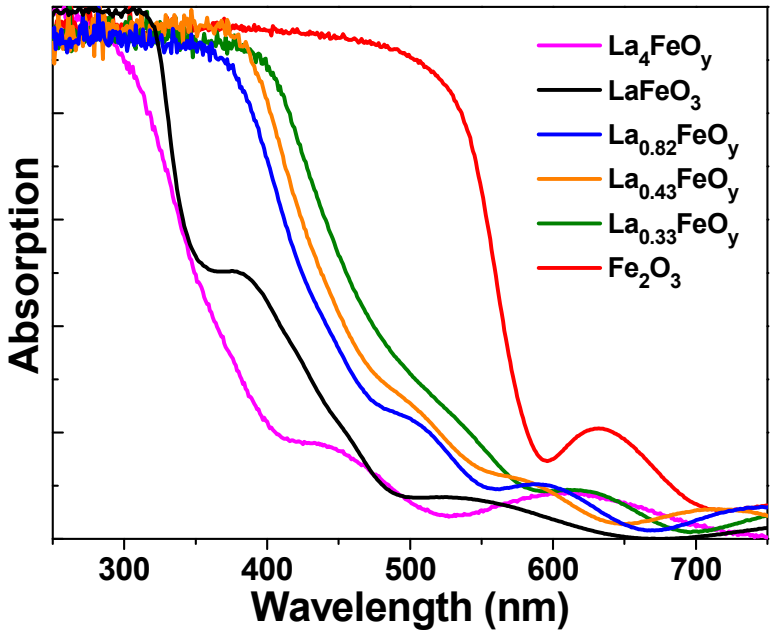

Fig. 2. UV-visible absorption spectra of La_4FeO_y, $LaFeO_3$, $La_{0.82}FeO_y$, $La_{0.43}FeO_y$, $La_{0.33}FeO_y$ and Fe_2O_3 films.

Linear sweep voltammetry (J-V) curves of $La_{1-x}FeO_y$ films were recorded under simulated sunlight illumination and a chopped beam was used to acquire both dark current and photocurrent in a single scan (Fig. 3a). The steady state photocurrent onset potential was around 0.6 V vs reversible hydrogen electrode (RHE) and the dark current remained stable until about 0.3 V vs RHE. All samples show an increase in negative current under illumination for potentials close to 0 V vs RHE, which corresponds to the behaviour of photocathodes. To determine the composition giving the highest PEC performance, chronoamperometric measurements under chopped illumination were conducted at a fixed potential of 0.3 V vs RHE (Fig. 3b). This potential value was chosen to obtain a dark current close to 0 µA. Fig. 3c shows the photocurrent density in absolute value as a function of the La stoichiometry of the films. These values have been determined at t = 525 s, i.e. in the middle of a light exposure period, when the spike corresponding to the formation of a double layer has passed, and after around 9 min of measurement, confirming the high stability of non-stoichiometric films. The photocurrent measured for group 1 films (high Fe excess) and for group 3 films (compositions close to $LaFeO_3$) is almost similar with values close to -1.8 $\mu A \cdot cm^{-2}$. The group 2 samples (intermediate compositions) exhibit much higher photocurrents, with a maximum value of -6.40 $\mu A \cdot cm^{-2}$ reached for the $La_{0.43}FeO_y$ film. The photocurrent density is ca. 3.5 higher for the non-stoichiometric $La_{0.43}FeO_y$ film compared to the stoichiometric $LaFeO_3$ film synthesized under the same experimental conditions. As the photogenerated current density shows a markedly enhanced value for the $La_{0.43}FeO_y$ film, a specific study will be focused on this film to further optimise its PEC performances by adjusting thermal annealing step and film thickness *(vide infra)*.

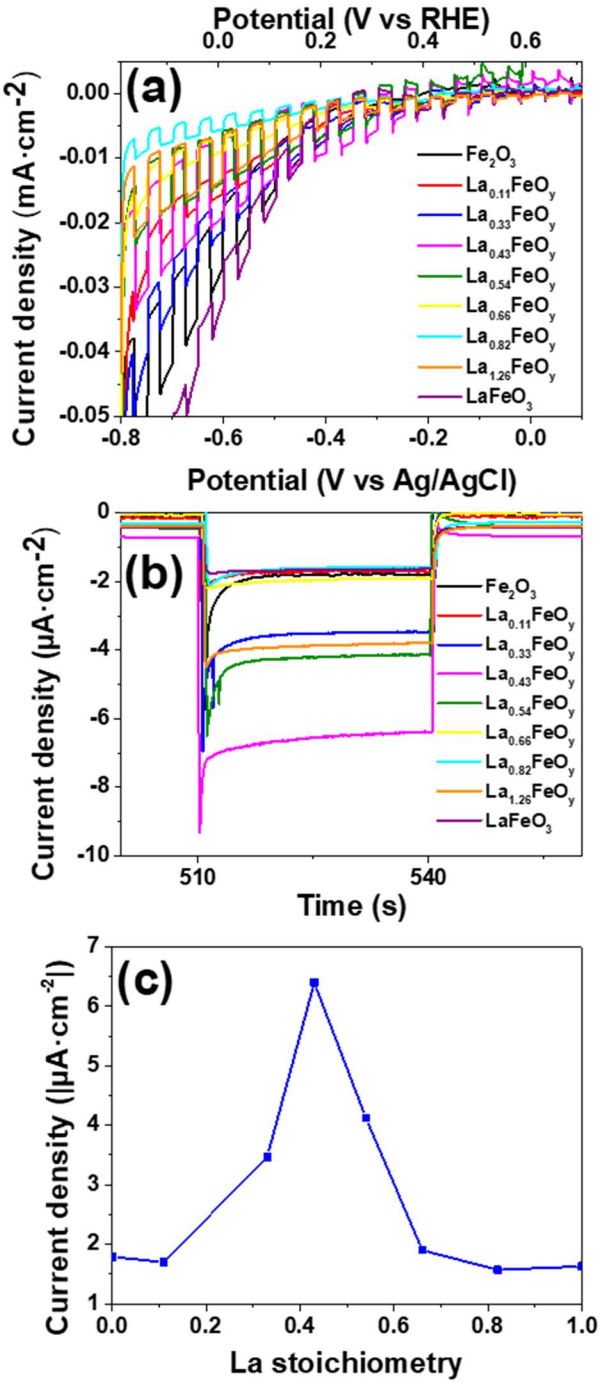

Fig. 3. (a) Current-potential curves and (b) current-time curves at a constant potential of 0.3 V vs RHE for the different $La_{1-x}FeO_y$ thin films under chopped illumination. (c) Photocurrent densities (absolute value) as a function of x' in $La_{x'}FeO_y$ films (0.1 M Na_2SO_4, pH 7, 1 sun).

As previously indicated, XRD patterns showed that the group 2 samples (with a slight excess in Fe) remain amorphous after an oxidative treatment under air at 500°C for 2 h (Fig. 1). The XRD pattern of a film with a 500 nm thickness oxidized at 650°C for 2 h

in air is shown in Fig. 4a. The presence of peaks corresponding to $LaFeO_3$ can be observed, indicating the improved crystallinity after the thermal treatment at 650°C. The average grain size of the $La_{0.43}FeO_y$ film was estimated by the Scherrer's formula (Eq. 1). A representative length of coherence domains of $LaFeO_3$ crystallites of ca. 26 ± 2 nm was extracted using the peak corresponding to the (121) plane. A value of 39 ± 2 nm was obtained for a stoichiometric $LaFeO_3$ film after a 2 h oxidative treatment at 500°C [13]. Such a decrease was also observed for $La_{1-x}FeO_y$ nanoparticles synthesized via thermal decomposition of Fe and La nitrates and was attributed to the organization of excess Fe into FeO_6 octahedra at the surface which limit the grain growth [28]. Measurements of the photocurrent density under constant applied potential (0.3V vs RHE) shows a significant improvement for $La_{0.43}FeO_y$ films oxidized 650°C show an increase of 60% from -6.4 $\mu A \cdot cm^{-1}$ (500°C) to -10.2 $\mu A \cdot cm^{-1}$ (650°C) (Fig. 4b). This result can be attributed to a better electron transfer due to the improved crystallinity of the film.

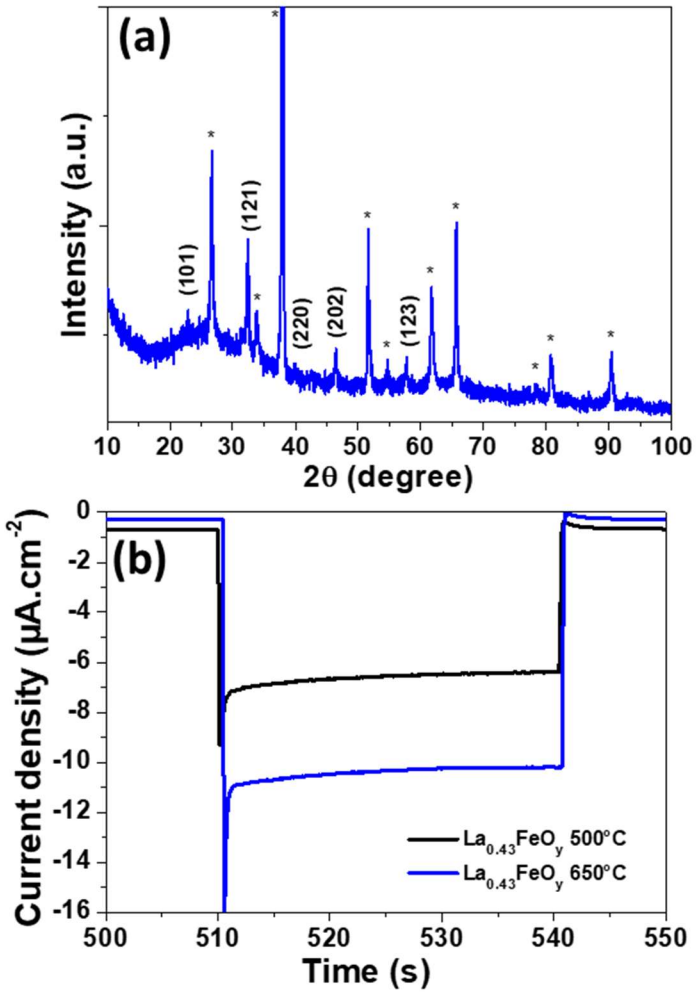

Fig. 4. (a) XRD pattern of the $La_{0.43}FeO_y$ sample after the *ex situ* oxidative treatment at 650°C for 2 h and (b) photocurrent density measurements of $La_{0,43}FeO_y$ films oxidized at 500 and 650°C (0.3 V vs RHE, 0,1M Na_2SO_4 pH 7, 1 sun).

To gain additional information on the phase distribution in these non-stoichiometric films, cross-sectional TEM analyses were performed on a $La_{0.43}FeO_y$ film (thickness of ca. 550 nm) deposited on a silicon substrate and oxidized at 650°C for 2 h. The bright field TEM image (Fig. 5a) and the corresponding EDS-STEM maps (Fig. S2) highlight an evolution of the composition and of the structure depending on the depth. The coating can be divided in 4 different zones (Fig. 5b). At the interface with the substrate, a thin layer (35-40 nm) with an excess of Fe (25 at.%) is observed (Zone 1).

EDS analyses show that the main part of the film (ca. 450 nm) contains Fe and La but with a higher concentration in La: 22 at.% Fe - 12 at.% La (Zone 2). However, an

evolution with the depth was noticed: close to the substrate, the composition is 13 at.% in La and 22 at.% in Fe, while on the other side, the composition is 11 at.% in La and 22 at.% in Fe. This evolution may originate from a diffusion of Fe atoms towards the interfaces during the oxidation treatment, which is consistent with the composition in zone 1 and zone 4. Noteworthy is that metal films synthesized by magnetron sputtering initially show a homogeneous composition in thickness (data not shown).

Close to the upper surface, a thin layer of about 60 nm containing a slightly higher atomic fraction in La (13% La and 21% Fe) was detected (Zone 3). Finally, the EDS-STEM maps (Fig. SI2) show the presence of a dense layer at the extreme surface (zone 4), composed only of Fe (30 at.%) and O (70 at.%).

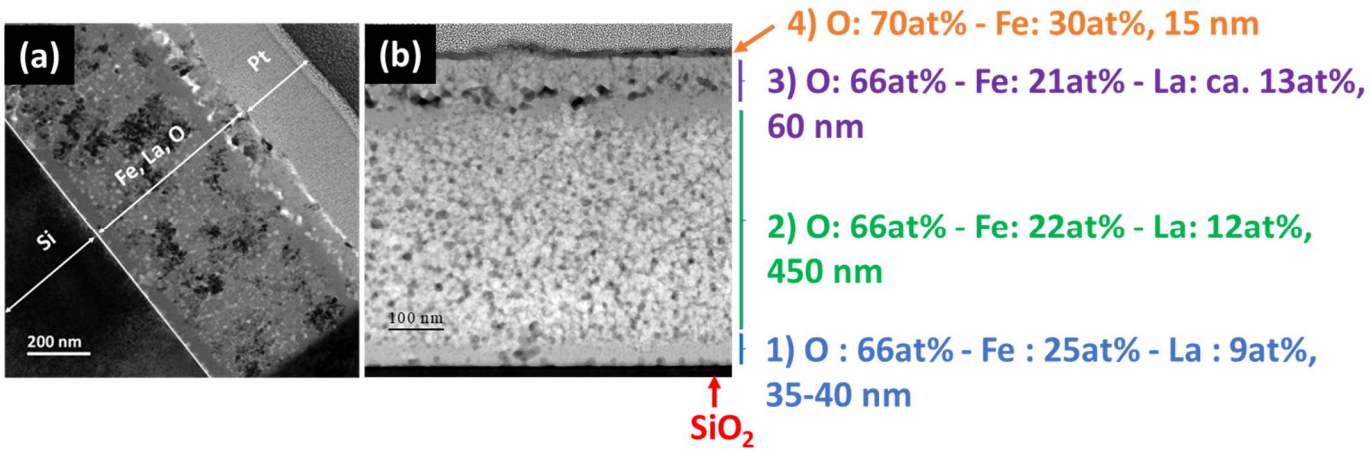

Fig. 5. (a) TEM cross sectional micrograph of a $La_{0.43}FeO_y$ film deposited on a Si substrate, after oxidation at 650°C for 2 h and (b) HAADF-STEM image showing the different zones and their composition.

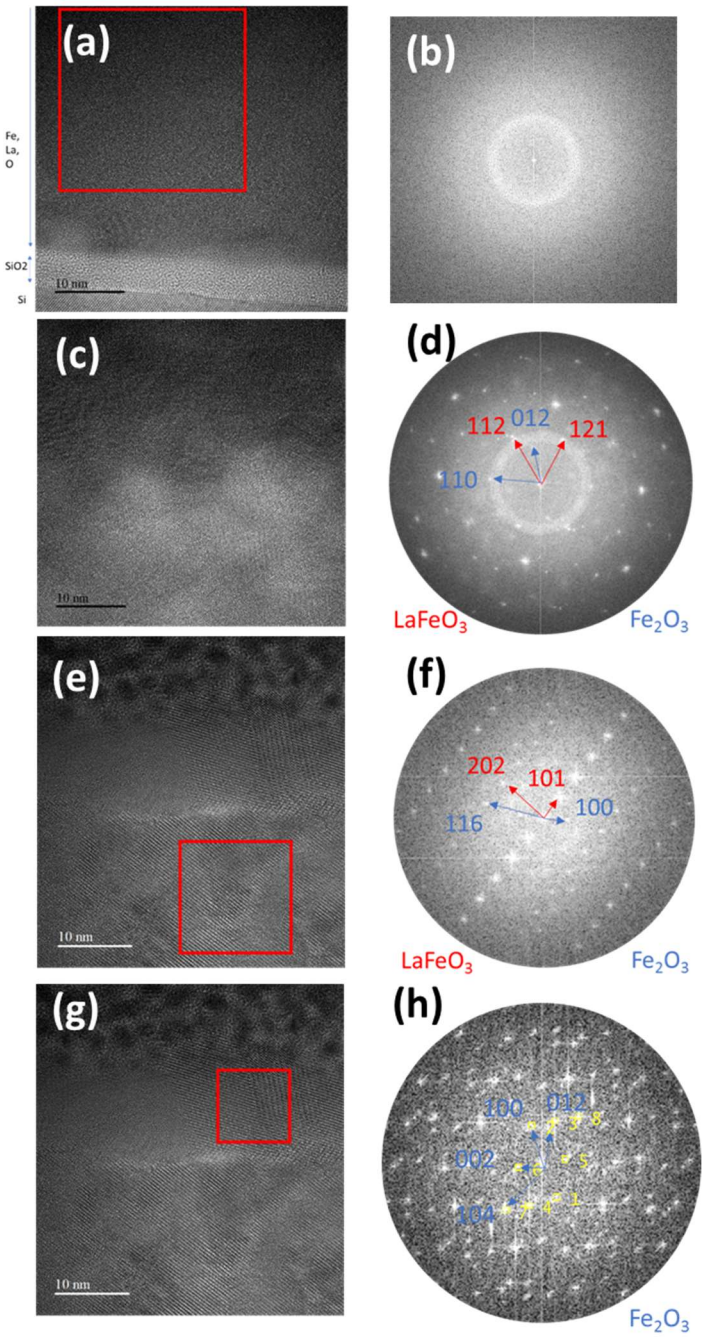

Fig. 6. High resolution TEM micrographs recorded in the 4 zones and their corresponding FFT patterns: (a) and (b) = zone 1, (c) and (d) = zone 2, (e) and (f) = zone 3, (g) and (h) = zone 4.

The high-resolution image and the corresponding Fast Fourier Transform (FFT) pattern recorded in zone 1 are characteristic of an amorphous phase (Fig. 6a and 6b). The bright field micrograph in zone 2 shows differences in contrast, the brighter areas likely originate from less dense or even porous regions (Fig. 6c). The corresponding FFT pattern shows a diffuse circle related to an amorphous phase as well as spots

characteristic of a polycrystalline material. The interplanar distances can be indexed to $LaFeO_3$ planes (orthorhombic Pnma) and to Fe_2O_3 planes (rhombohedral hematite R-3c) (Fig. 6d). As observed for zone 2, the spots observed in the FFT pattern recorded for zone 3 (red square) can also be indexed to $LaFeO_3$ and Fe_2O_3. However, the presence of a light diffuse circle suggests that an amorphous phase may also be present (Fig. 6e and 6f). In zone 4, at the upper surface, the spots observed on the FFT pattern correspond only to Fe_2O_3 (Fig. 6g and 6h). The organization in layers according to the depth of this non-stoichiometric film, summarized in Table 2, gives an average composition of 34 at.% La and 66 at.% Fe for the film, which is consistent with the composition estimated from EDS-SEM measurements.

Table 2. Composition, thickness, and structure of the different layers present in the $La_{0.43}FeO_y$ film.

Zone	Composition (at.%)	Thickness	Structure
1	O 66%, Fe 25%, La 9%	35-40 nm	Amorphous
2	O 66%, Fe 22%, La 12%	450 nm	Polycrystalline ($LaFeO_3$ and Fe_2O_3) + amorphous phase
3	O 66%, Fe 21%, La 13%	60 nm	Polycrystalline ($LaFeO_3$ and Fe_2O_3) + amorphous phase
4	O 70%, Fe30%, La 0%	15 nm	Fe_2O_3

An increase of the Fe amount was also observed on the surface of non-stoichiometric $LaFeO_3$ particles synthesized with a Fe excess [26,27]. This phenomenon seems to be similar to that described by Neagu *et al.* on non-stoichiometric perovskite particles of ABO_3 formula in which the deficiency in A leads to the formation of metallic or oxidized nanoparticles of B on the surface [37]. The presence of A deficiencies in the perovskite lattice decreases the stability of the crystal lattice and contributes to the spontaneous exsolution of B atoms to restore the stoichiometry in the lattice. The B atoms diffuse to the surface of the non-stoichiometric particles to form a shell [38]. This surface segregation phenomenon was also observed for $La_{0.6}Sr_{0.4}CoO_{3-\delta}$ films prepared by pulsed laser deposition and in Ti-doped $LaFeO_3$ particles [39–41]. This complex process of segregation leads to the formation of Fe_2O_3 layer at the surface of $LaFeO_3$ and allows significant improvements in the catalytic properties, as demonstrated for perovskite electrodes used in fuel cells [42,43]. An increase of the

temperature required to obtain the crystalline phase with modification of the perovskite structure was also observed by Porta *et al.* when doping $LaFeO_3$ with Mg [44].

3.2. Influence of $La_{0.43}FeO_y$ film thickness on the photoelectronic properties

To further optimize the photocatalytic activity, the influence of the thickness of the $La_{0.43}FeO_y$ film was investigated. Indeed, the thickness of the photoelectrodes is a key parameter in PEC measurements as it affects light absorption and thus the formation of electron/hole pairs, but also the charge carrier recombination probability [45]. The magnetron sputtering duration was adjusted to obtain film thicknesses of 50, 100, 250 and 500 nm after oxidation at 650°C for 2 h, all other experimental parameters being kept constant. Photocurrent measurements were carried out on FTO electrodes coated with $La_{0.43}FeO_y$ films (Fig. 7a). The 50, 250 and 500 nm thick-films showed almost similar results. The slight decrease in photocurrent generation for the 250 nm film may originate from changes of the crystal size or from a modification of the composition gradient, affecting photocatalytic properties. For a 100 nm thick $La_{0.43}FeO_y$ film, the photocurrent significantly increases by 57% compared to the 500 nm thick film synthesized in the same experimental conditions (-16 $\mu A \cdot cm^{-1}$ vs -10.2 $\mu A \cdot cm^{-1}$). Thus, a thickness of 100 nm appears to be optimal for this film composition for a further increase of the photoelectronic properties. The corresponding EIS Nyquist plots show a significant decrease in semi-circle diameter for the 100 nm thick layer compared to the 500 nm one, which indicates a decrease of the charge transfer resistance at the electrode/electrolyte interface (Fig. 7b).

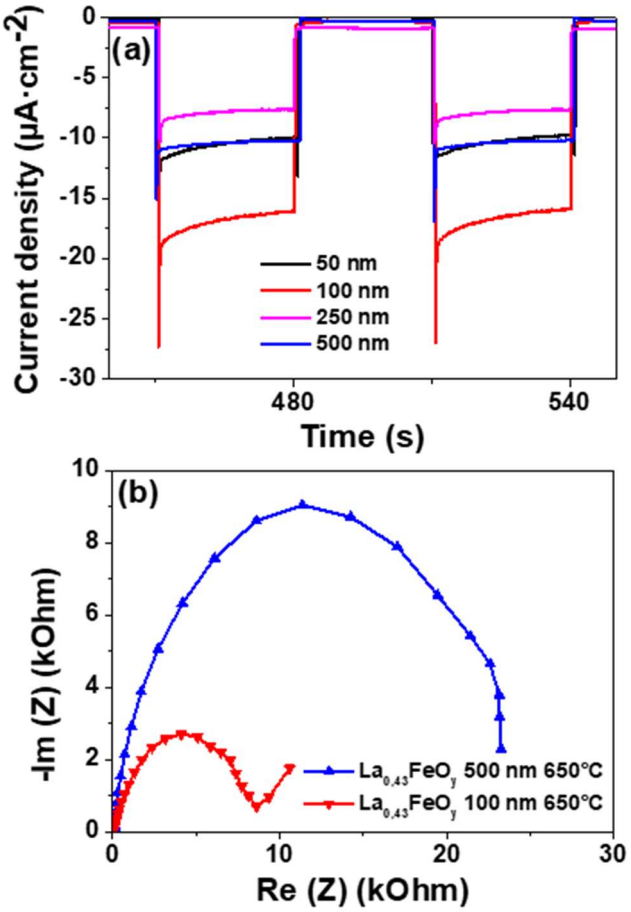

Fig. 7. (a) Current-time curves of $La_{0.43}FeO_y$ coated photoelectrodes at 0.3 V vs RHE under chopped illumination as a function of the film thickness and (b) EIS Nyquist plots of 500 and 100 nm thick $La_{0.43}FeO_y$ films (0.1M Na_2SO_4, pH 7, 1 sun).

3.3. Photoelectrocatalytic H_2 production

To confirm the improvement of the photocatalytic properties, measurements of H_2 production in a PEC cell were conducted. The production of H_2 from the photoelectrodes covered with a 100 nm thin layer of $La_{0.43}FeO_y$ or $LaFeO_3$ after oxidation was measured in a Na_2SO_4 solution (0.1 M) under irradiation of 1 sun (Xe lamp associated with an air mass filter AM 1.5G - 100 $mW.cm^{-2}$) (Fig. 8a). $LaFeO_3$ coated photoelectrodes showed an average H_2 production rate of 5.5 $\mu mol \cdot h^{-1} \cdot cm^{-2}$ once the stationary state was reached, i.e. between 2 and 7 h. The average production rate for $La_{0.43}FeO_y$, between 2 and 7 h, reached 11.2 $\mu mol\text{-}cm^{-2}$, which corresponds to an increase in H_2 production rate of 103%. These results further confirm the enhanced

photo(electro)catalytic activity by simply tuning the stoichiometry of the photocatalytic film. The performance of the $La_{0.43}FeO_y$ film is significantly improved compared to other photocathodes prepared with $LaFeO_3$ films, including a photocell composed of a $LaFeO_3$ photocathode and a Fe_2O_3 photoanode where H_2 production is close to 20 $\mu mol \cdot h^{-1}$ using a Xe lamp without AM 1.5G filter [45–47].

The simultaneous production of O_2 at the counter-electrode was also measured (Fig. 8b). An O_2 production rate of about 5.1 $\mu mol \cdot h^{-1} \cdot cm^{-2}$ was observed, corresponding to ca. the half of H_2 production as expected for the water splitting reaction. This quasi-stoichiometric production of H_2 and O_2 by PEC with a photocathode composed of a $La_{0.43}FeO_y$ film was confirmed by the pH stability of the electrolyte. Only a slight decrease was observed during the 7 h of irradiation (from 7.45 to 6.80), indicating that the concentration of H^+ and OH^- ions present in the solution remained almost constant. The stability of $La_{0.43}FeO_y$ film was also confirmed by chronoamperometric measurements (at 0.3 V vs RHE) over 10 h under a continuous simulated sunlight illumination and the photocurrent density was found to remain almost constant (Fig. S3). The non-stoichiometric composition leading to exsolution and segregation mechanisms observed during the thermal oxidation process has no influence on the stability of photoelectrodes, which is a key parameter for their practical application.

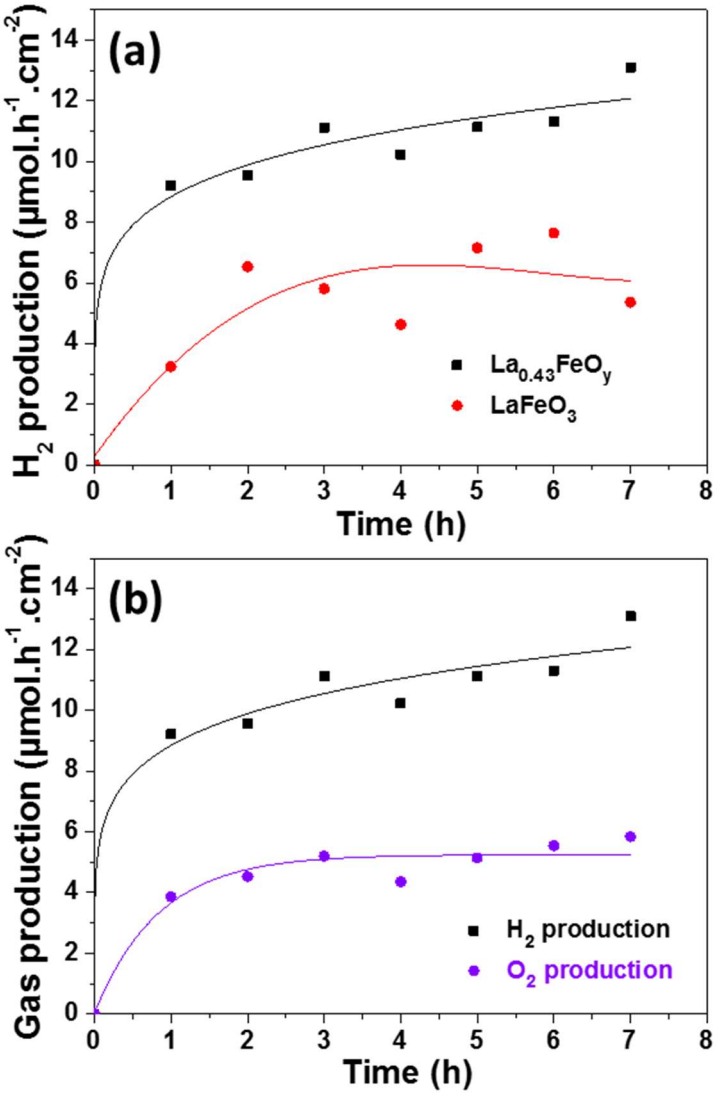

Fig. 8. (a) H_2 production rates of 100 nm $LaFeO_3$ and $La_{0.43}FeO_y$ oxidized films coated photoelectrodes, (b) H_2 and O_2 production rate evolutions of $La_{0.43}FeO_y$ photoelectrode (0.3 V vs RHE, 0.1 M Na_2SO_4, pH 7, 1 sun).

3.4. PEC mechanism

The Fe excess in $La_{1-x}FeO_y$ films was shown to produce Fe_2O_3 crystallites within the film by exsolution. Moreover, a Fe_2O_3 thin layer grows at the upper surface during thermal oxidation as observed by TEM. Therefore, the formation of a heterojunction between $LaFeO_3$ and Fe_2O_3 can be assumed.

The edge potentials of the valence band (VB) and conduction band (CB) of Fe_2O_3 were estimated using the semi-empirical calculation from Mulliken's electronegativity at the

point of zero-charge. Using the experimentally determined optical bandgap energy (Fig. S1b), E_{CB} and E_{VB} values of 0.3 and 2.48 V vs RHE were determined, respectively. The band edge potentials of $LaFeO_3$ were experimentally determined by EIS and from the bandgap estimated from UV-visible absorption measurements [13]. The positions of the VB edges of Fe_2O_3 and $LaFeO_3$ were used to estimate the band energy positions before contact (Fig. 9a). Within the film and at the upper surface, the heterojunction formed between the two semiconductors will favour a shift of band energies and at the junction, the Fermi levels of both semiconductors are equal and constant under equilibrium conditions. As a consequence, an electric field can be generated at the interface between Fe_2O_3 and $LaFeO_3$ leading to a better separation of the electron/hole pairs and thus to a reduction of their recombination probability.

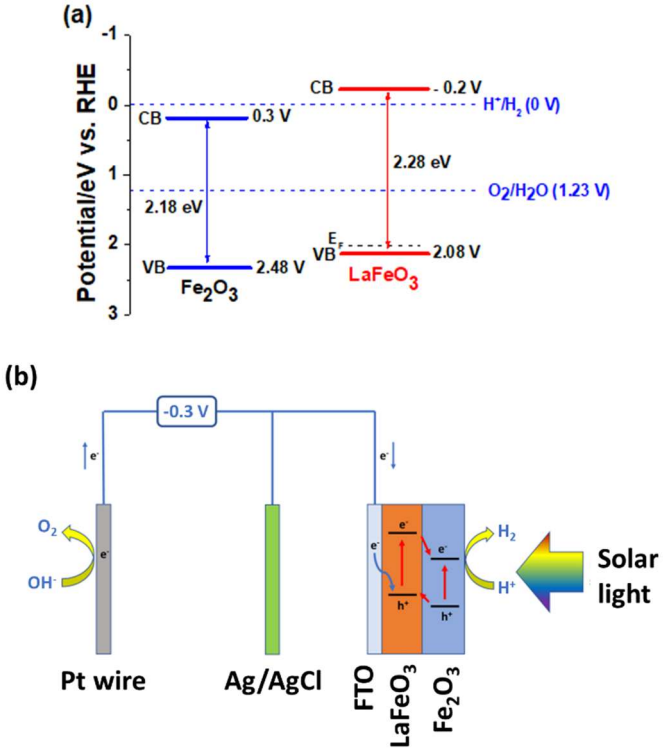

Fig. 9. (a) Diagram of band energy positions of Fe_2O_3 and $LaFeO_3$ before contact and (b) schematic representation of the separation and transfer pathway of photogenerated charge carriers for PEC H_2 production using $La_{0.43}FeO_y$ films under solar illumination.

The presence of a Fe_2O_3 surface layer could lead to the formation of type II heterojunction with a transfer of photogenerated electrons from the CB of the $LaFeO_3$ layer to the CB of Fe_2O_3 and simultaneously a transfer of holes from the VB of Fe_2O_3

to the VB of $LaFeO_3$ (Fig. 9b). The electrons photogenerated in Fe_2O_3 combined to those transferred from the CB of $LaFeO_3$ likely reach an excited level in the CB of Fe_2O_3 with a potential sufficiently negative to allow the reduction of water into hydrogen (Fig. 9a). Similar results were previously described for heterojunctions composed of NiO or CuO_x underneath a thin WO_3 layer [48,49]. Furthermore, the presence of Fe_2O_3 crystals within the film, as demonstrated by TEM measurements, could also improve the bulk charge transfer, reducing their recombination probability before reaching the surface.

4. Conclusion

The influence of the stoichiometry in $La_{1-x}FeO_y$ films on their photocatalytic activity for H_2 production was investigated. The modification of the power applied to the metallic targets during magnetron co-sputtering process allows a fine control of the film composition. The highest photoactivity was observed for a 100 nm-thick $La_{0.43}FeO_y$ film oxidized at 650°C for 2 h.

TEM analyses show the presence of $LaFeO_3$ within the film, underneath a thin (15 nm) and continuous polycrystalline Fe_2O_3 layer at the upper surface. The presence of Fe_2O_3 originates from an exsolution mechanism typically observed for non-stoichiometric perovskites. The improvement of the photocatalytic properties by optimizing the stoichiometry, the oxidation temperature and the film thickness was confirmed by a large increase of H_2 production rates by comparison with a stoichiometric $LaFeO_3$ film prepared under the same experimental conditions: from 5.5 to 11.2 $\mu mol \cdot cm^{-2}$, i.e. 103%. This increase in catalytic performances associated to the high stability, visible light photoactivation and facile, low cost and scalable synthesis process make $La_{0.43}FeO_y$ films of high interest as photocathode for PEC water splitting systems.

CRediT authorship contribution statement

V. Guigoz: Investigation, Writing - original draft. **S. Bruyère:** Investigation, Writing - review & editing. **S. Migot:** Investigation, Writing - review & editing. **R. Schneider:** Supervision, Funding acquisition, Writing - review & editing. **T. Gries:** Supervision, Funding acquisition, Writing - review & editing.

Declaration of Competing Interest

The authors declare that they have no known competing financial interests or personal relationships that could have appeared to influence the work reported in this paper.

Acknowledgements

This work was supported partly by the French PIA project « Lorraine Université d'Excellence », reference ANR-15-IDEX-04-LUE.

Appendix A. Supplementary data

Supplementary data to this article can be found at http://doi.org/

References

[1] Züttel Andreas, Remhof Arndt, Borgschulte Andreas, Friedrichs Oliver, Hydrogen: the future energy carrier, Philos. Trans. R. Soc. Math. Phys. Eng. Sci. 368 (2010) 3329–3342. https://doi.org/10.1098/rsta.2010.0113.

[2] K. Mazloomi, C. Gomes, Hydrogen as an energy carrier: Prospects and challenges, Renew. Sustain. Energy Rev. 16 (2012) 3024–3033. https://doi.org/10.1016/j.rser.2012.02.028.

[3] X. Xu, Y. Chen, W. Zhou, Z. Zhu, C. Su, M. Liu, Z. Shao, A Perovskite Electrocatalyst for Efficient Hydrogen Evolution Reaction, Adv. Mater. 28 (2016) 6442–6448. https://doi.org/10.1002/adma.201600005.

[4] M. Grätzel, Photoelectrochemical cells, Nature. 414 (2001) 338–344. https://doi.org/10.1038/35104607.

[5] Y. Lin, G. Yuan, R. Liu, S. Zhou, S.W. Sheehan, D. Wang, Semiconductor nanostructure-based photoelectrochemical water splitting: A brief review, Chem. Phys. Lett. 507 (2011) 209–215. https://doi.org/10.1016/j.cplett.2011.03.074.

[6] B.Y. Alfaifi, H. Ullah, S. Alfaifi, A.A. Tahir, T.K. Mallick, Photoelectrochemical solar water splitting: From basic principles to advanced devices, Veruscript Funct. Nanomater. 2 (2018) BDJOC3. https://doi.org/10.22261/FNAN.BDJOC3.

[7] S. Piccinin, The band structure and optical absorption of hematite (α-Fe_2O_3): a first-principles GW-BSE study, Phys. Chem. Chem. Phys. 21 (2019) 2957–2967. https://doi.org/10.1039/C8CP07132B.

[8] W. Wang, M. Xu, X. Xu, W. Zhou, Z. Shao, Perovskite Oxide Based Electrodes for High-Performance Photoelectrochemical Water Splitting, Angew. Chem. Int. Ed. 59 (2020) 136–152. https://doi.org/10.1002/anie.201900292.

[9] P. Kanhere, Z. Chen, A Review on Visible Light Active Perovskite-Based Photocatalysts, Molecules. 19 (2014) 19995–20022. https://doi.org/10.3390/molecules191219995.

[10] M. Ismael, M. Wark, Perovskite-type $LaFeO_3$: Photoelectrochemical Properties and Photocatalytic Degradation of Organic Pollutants Under Visible Light Irradiation, Catalysts. 9 (2019) 342. https://doi.org/10.3390/catal9040342.

[11] Y. Tao, L. Wu, X. Zhao, X. Chen, R. Li, M. Chen, et al. Strong Hollow Spherical La_2 NiO_4 Photocatalytic Microreactor for Round-the-Clock Environmental

Remediation. ACS Appl. Mater. Interfaces 11 (2019) 25967–75. https://doi.org/10.1021/acsami.9b07216.
[12] M.I. Díez-García, R. Gómez, Metal Doping to Enhance the Photoelectrochemical Behavior of $LaFeO_3$ Photocathodes, ChemSusChem. 10 (2017) 2457–2463. https://doi.org/10.1002/cssc.201700166.
[13] V. Guigoz, L. Balan, A. Aboulaich, R. Schneider, T. Gries, Heterostructured thin $LaFeO_3$/g-C_3N_4 films for efficient photoelectrochemical hydrogen evolution, Int. J. Hydrog. Energy. 45 (2020) 17468–17479. https://doi.org/10.1016/j.ijhydene.2020.04.267.
[14] V. Celorrio, K. Bradley, O.J. Weber, S.R. Hall, D.J. Fermín, Photoelectrochemical Properties of $LaFeO_3$ Nanoparticles, ChemElectroChem. 1 (2014) 1667–1671. https://doi.org/10.1002/celc.201402192.
[15] P. Kanhere, J. Nisar, Y. Tang, B. Pathak, R. Ahuja, J. Zheng, Z. Chen, Electronic Structure, Optical Properties, and Photocatalytic Activities of $LaFeO_3$ –$NaTaO_3$ Solid Solution, J. Phys. Chem. C. 116 (2012) 22767–22773. https://doi.org/10.1021/jp307857h.
[16] G.P. Wheeler, K.-S. Choi, Photoelectrochemical Properties and Stability of Nanoporous p-Type $LaFeO_3$ Photoelectrodes Prepared by Electrodeposition, ACS Energy Lett. 2 (2017) 2378–2382. https://doi.org/10.1021/acsenergylett.7b00642.
[17] Q. Peng, J. Wang, Y.W. Wen, B. Shan, R. Chen, Surface modification of $LaFeO_3$ by Co-Pi electrochemical deposition as an efficient photoanode under visible light, RSC Adv. 6 (2016) 26192–26198. https://doi.org/10.1039/C6RA01810F.
[18] S. Li, L. Jing, W. Fu, L. Yang, B. Xin, H. Fu, Photoinduced charge property of nanosized perovskite-type $LaFeO_3$ and its relationships with photocatalytic activity under visible irradiation, Mater. Res. Bull. 42 (2007) 203–212. https://doi.org/10.1016/j.materresbull.2006.06.010.
[19] R. Hu, C. Li, X. Wang, Y. Sun, H. Jia, H. Su, Y. Zhang, Photocatalytic activities of $LaFeO_3$ and La_2FeTiO_6 in p-chlorophenol degradation under visible light, Catal. Commun. 29 (2012) 35–39. https://doi.org/10.1016/j.catcom.2012.09.012.
[20] S. Thirumalairajan, K. Girija, N.Y. Hebalkar, D. Mangalaraj, C. Viswanathan, N. Ponpandian, Shape evolution of perovskite $LaFeO_3$ nanostructures: a systematic investigation of growth mechanism, properties and morphology dependent photocatalytic activities, RSC Adv. 3 (2013) 7549–7561. https://doi.org/10.1039/C3RA00006K.
[21] J. Low, J. Yu, M. Jaroniec, S. Wageh, A.A. Al-Ghamdi, Heterojunction Photocatalysts, Adv. Mater. 29 (2017) 1601694. https://doi.org/10.1002/adma.201601694.
[22] S.J.A. Moniz, S.A. Shevlin, D.J. Martin, Z.-X. Guo, J. Tang, Visible-light driven heterojunction photocatalysts for water splitting – a critical review, Energy Environ. Sci. 8 (2015) 731–759. https://doi.org/10.1039/C4EE03271C.
[23] M. Ge, J. Cai, J. Iocozzia, C. Cao, J. Huang, X. Zhang, J. Shen, S. Wang, S. Zhang, K.-Q. Zhang, Y. Lai, Z. Lin, A review of TiO_2 nanostructured catalysts for sustainable H_2 generation, Int. J. Hydrog. Energy. 42 (2017) 8418–8449. https://doi.org/10.1016/j.ijhydene.2016.12.052.
[24] V. Kumaravel, S. Mathew, J. Bartlett, S.C. Pillai, Photocatalytic hydrogen production using metal doped TiO_2: A review of recent advances, Appl. Catal. B Environ. 244 (2019) 1021–1064. https://doi.org/10.1016/j.apcatb.2018.11.080.

[25] H. Zhang, Z. Luo, Y. Liu, Y. Jiang. Noble-metal-free Ni_3C as co-catalyst on $LaNiO_3$ with enhanced photocatalytic activity. Appl. Catal. B Environ. 277 (2020) 119166. https://doi.org/10.1016/j.apcatb.2020.119166.
[26] J. Faye, A. Baylet, M. Trentesaux, S. Royer, F. Dumeignil, D. Duprez, S. Valange, J.-M. Tatibouët, Influence of lanthanum stoichiometry in $La_{1-x}FeO_{3-\delta}$ perovskites on their structure and catalytic performance in CH4 total oxidation, Appl. Catal. B Environ. 126 (2012) 134–143. https://doi.org/10.1016/j.apcatb.2012.07.001.
[27] A. Schön, J.-P. Dacquin, P. Granger, C. Dujardin, Non stoichiometric $La_{1-y}FeO_3$ perovskite-based catalysts as alternative to commercial three-way-catalysts? – Impact of Cu and Rh doping, Appl. Catal. B Environ. 223 (2018) 167–176. https://doi.org/10.1016/j.apcatb.2017.06.026.
[28] A. Delmastro, D. Mazza, S. Ronchetti, M. Vallino, R. Spinicci, P. Brovetto, M. Salis, Synthesis and characterization of non-stoichiometric $LaFeO_3$ perovskite, Mater. Sci. Eng. B. 79 (2001) 140–145. https://doi.org/10.1016/S0921-5107(00)00570-5.
[29] Noble Materials for Photoelectrochemical Water Splitting, in: Mater. Res. Found., 1st ed., Materials Research Forum LLC, 2020: pp. 183–213. https://doi.org/10.21741/9781644900734-7.
[30] M.D. Bhatt, J.Y. Lee, Advancement of Platinum (Pt)-Free (Non-Pt Precious Metals) and/or Metal-Free (Non-Precious Metals) Electrocatalysts in Energy Applications: A Review and Perspectives, Energy Fuels. 34 (2020) 6634-6695. https://doi.org/10.1021/acs.energyfuels.0c00953.
[31] M.D. Scafetta, A.M. Cordi, J.M. Rondinelli, S.J. May, Band structure and optical transitions in $LaFeO_3$: theory and experiment, J. Phys. Condens. Matter. 26 (2014) 505502. https://doi.org/10.1088/0953-8984/26/50/505502.
[32] A. Pandey, G. Jain, D. Vyas, S. Irusta, S. Sharma, Nonreducible, Basic La_2O_3 to Reducible, Acidic $La_{2-x}Sb_xO_3$ with Significant Oxygen Storage Capacity, Lower Band Gap, and Effect on the Catalytic Activity, J. Phys. Chem. C. 121 (2017) 481–489. https://doi.org/10.1021/acs.jpcc.6b10821.
[33] R.S. Gedam, D.D. Ramteke, Electrical, dielectric and optical properties of La_2O_3 doped lithium borate glasses, J. Phys. Chem. Solids. 74 (2013) 1039–1044. https://doi.org/10.1016/j.jpcs.2013.03.001.
[34] A.A. Yadav, A.C. Lokhande, C.D. Lokhande, A simple chemical route for synthesis of microrods-like La_2O_3 thin films, Mater. Lett. 160 (2015) 500–502. https://doi.org/10.1016/j.matlet.2015.07.083.
[35] H. Nohira, T. Shiraishi, K. Takahashi, T. Hattori, I. Kashiwagi, C. Ohshima, S. Ohmi, H. Iwai, S. Joumori, K. Nakajima, M. Suzuki, K. Kimura, Atomic-scale depth profiling of composition, chemical structure and electronic band structure of La_2O_3/Si(100) interfacial transition layer, Appl. Surf. Sci. 234 (2004) 493–496. https://doi.org/10.1016/j.apsusc.2004.05.032.
[36] Q.-Y. Liu, Z.-B. Fang, T. Ji, S.-Y. Liu, Y.-S. Tan, J.-J. Chen, Y.-Y. Zhu, Band Alignment and Band Gap Characterization of La_2O_3 Films on Si Substrates Grown by Radio Frequency Magnetron Sputtering, Chin. Phys. Lett. 31 (2014) 027702. https://doi.org/10.1088/0256-307X/31/2/027702.
[37] D. Neagu, G. Tsekouras, D.N. Miller, H. Ménard, J.T.S. Irvine, In situ growth of nanoparticles through control of non-stoichiometry, Nat. Chem. 5 (2013) 916–923. https://doi.org/10.1038/nchem.1773.
[38] O. Kwon, S. Sengodan, K. Kim, G. Kim, H.Y. Jeong, J. Shin, Y.-W. Ju, J.W. Han, G. Kim, Exsolution trends and co-segregation aspects of self-grown catalyst

nanoparticles in perovskites, Nat. Commun. 8 (2017) 15967. https://doi.org/10.1038/ncomms15967.
[39] M. Kubicek, A. Limbeck, T. Frömling, H. Hutter, J. Fleig, Relationship between Cation Segregation and the Electrochemical Oxygen Reduction Kinetics of $La_{0.6}Sr_{0.4}CoO_{3-\delta}$ Thin Film Electrodes, J. Electrochem. Soc. 158 (2011) B727. https://doi.org/10.1149/1.3581114.
[40] Y. Chen, H. Téllez, M. Burriel, F. Yang, N. Tsvetkov, Z. Cai, D.W. McComb, J.A. Kilner, B. Yildiz, Segregated Chemistry and Structure on (001) and (100) Surfaces of $(La_{1-x}Sr_x)_2CoO_4$ Override the Crystal Anisotropy in Oxygen Exchange Kinetics, Chem. Mater. 27 (2015) 5436–5450. https://doi.org/10.1021/acs.chemmater.5b02292.
[41] P. Garcia-Muñoz, F. Fresno, C. Lefevre, D. Robert, N. Keller. Synergy effect between photocatalysis and heterogeneous photo-Fenton catalysis on Ti-doped $LaFeO_3$ perovskite for high efficiency light-assisted water treatment. Catal. Sci. Technol. 10 (2020) 1299–310. https://doi.org/10.1039/C9CY02269D.
[42] D. Chen, C. Chen, Z.M. Baiyee, Z. Shao, F. Ciucci, Nonstoichiometric Oxides as Low-Cost and Highly-Efficient Oxygen Reduction/Evolution Catalysts for Low-Temperature Electrochemical Devices, Chem. Rev. 115 (2015) 9869–9921. https://doi.org/10.1021/acs.chemrev.5b00073.
[43] Y. Li, W. Zhang, Y. Zheng, J. Chen, B. Yu, Y. Chen, M. Liu, Controlling cation segregation in perovskite-based electrodes for high electro-catalytic activity and durability, Chem. Soc. Rev. 46 (2017) 6345–6378. https://doi.org/10.1039/C7CS00120G.
[44] P. Porta, S. Cimino, S. De Rossi, M. Faticanti, G. Minelli, I. Pettiti, $AFeO_3$ (A=La, Nd, Sm) and $LaFe_{1-x}Mg_xO_3$ perovskites: structural and redox properties, Mater. Chem. Phys. 71 (2001) 165–173. https://doi.org/10.1016/S0254-0584(01)00273-5.
[45] G.S. Pawar, A.A. Tahir, Unbiased Spontaneous Solar Fuel Production using Stable $LaFeO_3$ Photoelectrode, Sci. Rep. 8 (2018) 3501. https://doi.org/10.1038/s41598-018-21821-z.
[46] Q. Yu, X. Meng, T. Wang, P. Li, L. Liu, K. Chang, G. Liu, J. Ye, A highly durable p-$LaFeO_3$/n-Fe_2O_3 photocell for effective water splitting under visible light, Chem. Commun. 51 (2015) 3630–3633. https://doi.org/10.1039/C4CC09240F.
[47] F. Li, R. Xu, C. Nie, X. Wu, P. Zhang, L. Duan, L. Sun, Dye-sensitized $LaFeO_3$ photocathode for solar-driven H_2 generation, Chem. Commun. 55 (2019) 12940–12943. https://doi.org/10.1039/C9CC06781G.
[48] P. Wu, Z. Liu, D. Chen, M. Zhou, J. Wei, Flake-like NiO/WO_3 p-n heterojunction photocathode for photoelectrochemical water splitting, Appl. Surf. Sci. 440 (2018) 1101–1106. https://doi.org/10.1016/j.apsusc.2018.01.292.
[49] T. Xie, T. Zheng, R. Wang, T. Pu, X. Li, Y. Bu, J.-P. Ao, A promising CuO_x/WO_3 p-n heterojunction thin-film photocathode fabricated by magnetron reactive sputtering, Int. J. Hydrog. Energy. 44 (2019) 4062–4071. https://doi.org/10.1016/j.ijhydene.2018.12.153.